SPATIAL-FREQUENCY SYNERGY FOR REMOTE SENSING IMAGE SUPER-RESOLUTION WITH HOLISTIC FEATURE ENHANCEMENT

Anonymous authors
Paper under double-blind review

ABSTRACT

High-resolution (HR) remote sensing images are essential for various applications of Earth observation, but hardware limitations generally give rise to low-resolution (LR) and degraded acquisitions. Super-resolution (SR) has currently emerged as a popular manner to ease this issue. However, most existing SR methods fail to effectively exploit the synergy between frequency and spatial information, while also suffering from inadequate feature enhancement. In this work, we present a novel model for remote sensing image SR, termed as Spatial-Frequency Synergy Network (SFSN). Firstly, it holistically boosts hierarchical features from both the channel and spatial dimensions, through Adaptive Channel Shifting (AdaCS) and Multi-Scale Large Kernel Attention (MS-LKA), respectively. Meanwhile, we also devise a Dual-Domain Interaction Attention (DDIA) to simulate the interaction between spatial and frequency domains explicitly, which enables synergic feature refinement and HR detail recovery. It also delivers a versatile solution for bridging the spatial-frequency domain gap in remote sensing SR. Extensive experiments on benchmark datasets have demonstrated the superiority of the proposed SFSN over advanced SR models quantitatively and qualitatively, while still maintaining considerably low overhead.

1 INTRODUCTION

High-resolution (HR) remote sensing images are essentially desired by a wide range of applications such as environment monitoring (Rau et al., 2014), resource exploration (Calvin et al., 2015), military reconnaissance (Wang et al., 2014) etc. However, the inherent limitations of satellite imaging hardware, transmission bandwidth, and challenging imaging environments typically lead to image degradations via resolution reduction, compression artifacts and information loss. The degradations impair critical visual features such as edge definition and fine details, substantially limiting the practical use of remote sensing images. In recent years, super-resolution (SR) has emerged as an efficient and effective alternative that can moderate the dilemma between imaging quality and overhead, which targets at recovering one HR image from its low-resolution (LR) observations.

For the task of remote sensing image SR (RSISR), deep learning methods, especially those based on convolutional neural networks (CNNs), have become a dominant solution in the field. Several representative works (Lei et al., 2017; Dong et al., 2020; Zhang et al., 2020; Lei & Shi, 2021; Wang et al., 2022) have been proposed and exhibited superior SR performance. Nevertheless, the intrinsic features of RSI, e.g., frequent recurrence of texture patterns and substantial heterogeneity of image structure, have exposed the inherent drawbacks of CNN-based approaches. The limited receptive field fails to capture long-range dependency while exhibiting insufficient adaptability to input variations, which impedes the generation of more representative features. Hence, more sophisticated models built on Transformers (Vaswani et al., 2017) have garnered increasing attention within the RSISR community (Wang et al., 2023d; Kang et al., 2024; Lei et al., 2021). Despite remarkable successes, Transformer-based methods are inclined to preserve low-frequency (LF) information while exhibiting deficient ability in recovering high-frequency (HF) details (Li et al., 2025a). Moreover, most of these SR models are computationally intensive, hindering their practical deployment in real-world applications.

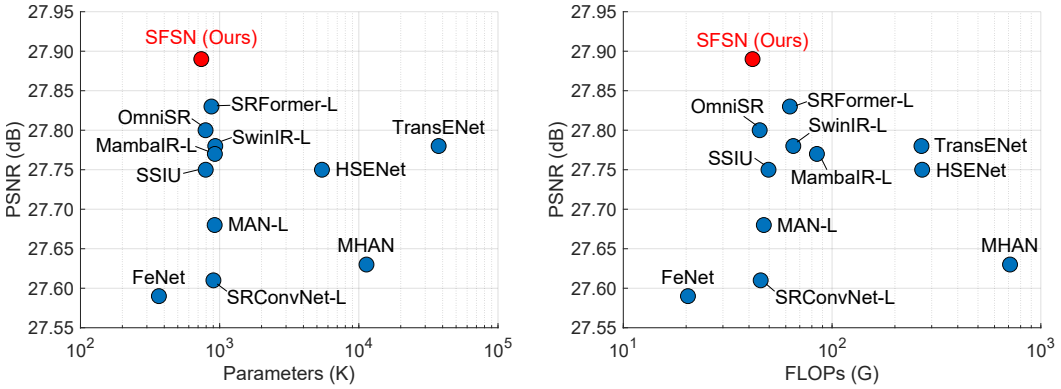

(a) PSNR (dB) vs. Parameters (K) (b) PSNR (dB) vs. FLOPs (G)

Figure 1: Comparison between performance and overhead of typical RSISR models on UCMerced with SR×4. Our SFSN achieves the best results with the second-lowest cost.

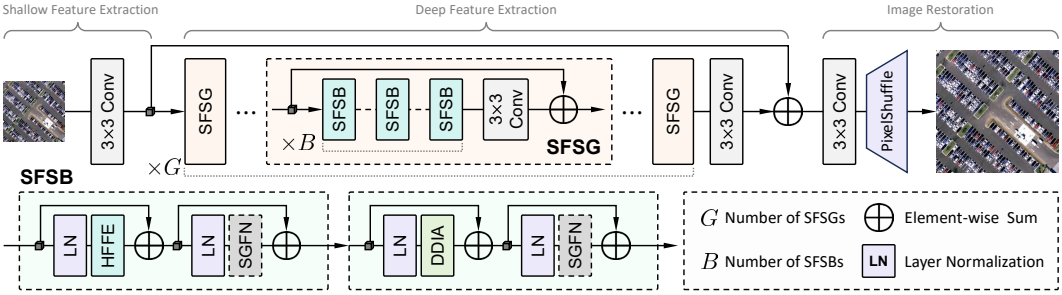

Figure 2: The overall architecture of our spatial-frequency synergy network (SFSN). Please refer to Fig. 3 and Fig. 4 for the description of our HFFE and DDIA.

Lightweight design serves as a straightforward approach to relax computational overhead, yet how to enhance model performance under constrained network resources remains an underexplored issue. Feature enhancement is a common strategy for facilitating the performance of lightweight deep models. For RSISR tasks, feature enhancement can provide more diverse features for model inference (Zhang et al., 2023) or expand the effective receptive field (ERF) of the model (Zhao et al., 2024; Li et al., 2025c), thereby improving the trade-off between model performance and cost. However, most existing approaches only consider enhancing features from either the spatial or channel dimension, failing to fully incorporate omnidirectional feature augmentation or establish effective integration strategies, which undesirably results in underexplored model capability.

Recent advances in RSISR have brought several methods (Wang et al., 2024a; Xiao et al., 2024) that fuse spatial and frequency features to enhance the capacity of SR models for accurately recovering HF structural and textural details. This dual-domain strategy can alleviate the inherent limitations of single-domain processing, i.e., *spatial features often fail to capture global information while frequency components struggle to model spatial relationships*. Nevertheless, most existing SR methods combining both spatial and frequency domains have not sufficiently explored effective strategies to harness complementary features, therefore limiting the potential for promoting model performance.

To this end, we propose a novel model in this work, which is termed as spatial-frequency synergy network (SFSN) and advances RSISR with two components: (1) holistic feature enhancement and (2) synergy inference between the spatial and frequency domains. The former adopts adaptive channel shifting (AdaCS) strategy along the channel dimension and multi-scale large-kernel attention (MS-LKA) in the spatial dimensions to enrich feature diversity and facilitate efficient model inference. The latter enables the model to reconcile long-term dependency and spatial relationship modeling via dual-domain interaction attention (DDIA). Our SFSN model achieves superior SR performance with modest parameters and costs, remarkably improving the performance-efficiency equilibrium as illustrated in Fig. 1. In summary, the main contributions of this work are as follows:

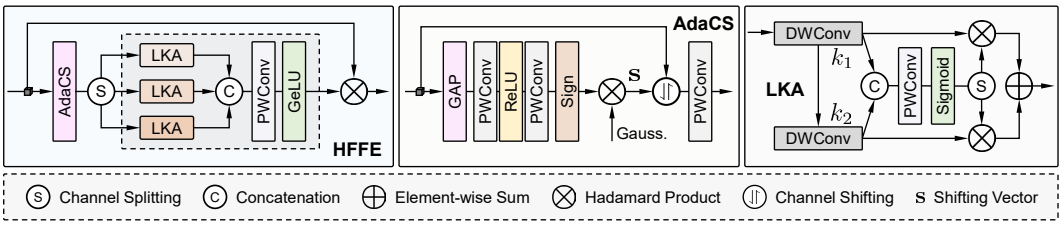

Figure 3: Structural components of our HFFE module. In AdaCS, shifting margins $(\Delta h, \Delta w)$ are determined by a Gaussian, while shifting directions are learned with a Sign$(\cdot)$ function.

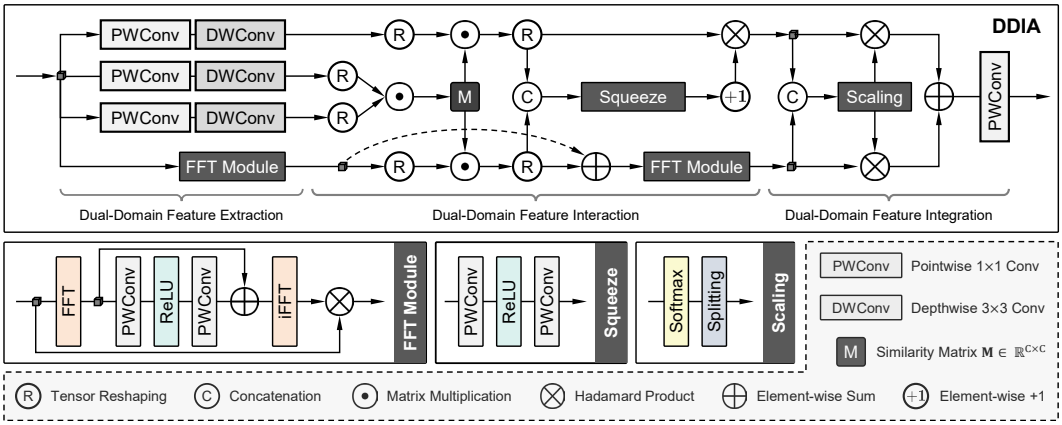

Figure 4: The diagram of our DDIA. It evolves from a typical self-attention coupled with a frequency mapping branch. Please note that the operation of element-wise +1 implies a residual shortcut.

- By considering holistic feature enhancement and spatial-frequency domain interaction, we propose a lightweight yet effective SFSN for RSISR tasks. Experimental results illustrate that our SFSN achieves better compromise between model performance and overhead.
- We present a holistic fusion feature enhancement (HFFE) strategy that integrates AdaCS and MS-LKA to potentiate hierarchical features from both channel and spatial dimensions.
- A dual-domain interaction attention (DDIA) is devised to simulate the correlation between spatial and frequency domains, enabling synergic spatial-frequency feature refinement.

2 Related Work

2.1 Remote Sensing Image Super-Resolution

Since Dong et al. (Dong et al., 2014) pioneered the usage of CNNs to single image super-resolution (SISR) and exhibited remarkable SR performance, there has been a proliferation of CNN-based methods for RSISR. Lei et al. (Lei et al., 2017) introduced LGCNet, which combines both local and global information for HR recovery. Haut et al. (Haut et al., 2019) and Dong et al. (Dong et al., 2020) incorporated residual units and skip connections to capture richer feature representation. Zhang et al. (Zhang et al., 2020) illustrated a high-order attention (HOA) module to exploit hierarchical features. Afterwards, Lei et al. (Lei & Shi, 2021) proposed to leverage multi-scale self-similarity (Glasner et al., 2009) with non-local attention. Moreover, Wang et al. (Wang et al., 2022) devised a lightweight FeNet that adopted channel splitting and weight sharing to decrease overhead.

Recently, more advanced models built upon Transformers (Vaswani et al., 2017) and Mamba (Guo et al., 2024) have garnered noteworthy attention in the RSISR community, and notably promoted the progress of RSISR. The representative works include TransNet (Lei et al., 2021), HAUNet (Wang et al., 2023d), ESTNet (Kang et al., 2024), as well as FMSR (Xiao et al., 2024) and ConvMambaSRF (Zhu et al., 2024). Although these models have made notable progresses in modeling long-range dependencies, they typically ignore the benefits of adequate feature enhancement for RSISR.

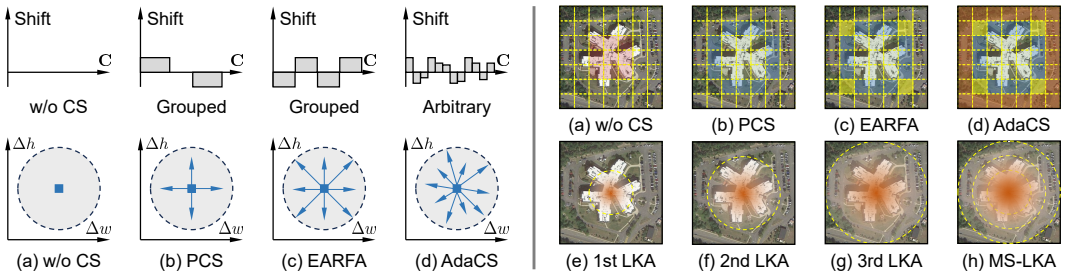

Figure 5: The diagram of our AdaCS (left) and the synergy with MS-LKA (right). Different from PCS (Zhang et al., 2023) and EARFA (Zhao et al., 2024), our AdaCS conducts channel shifting on non-grouped channels with arbitrary amplitude and direction. In collaboration with MS-LKA, our HFFE achieves holistic feature enhancement ((d) + (h) on the right side).

Furthermore, when the model scale is limited, the representational capability of the model has not been fully exploited, resulting in suboptimal trade-offs between model performance and overhead.

2.2 Feature Enhancement for SISR

Feature enhancement serves as a prevalent tool to augment the representational capacity of SR models by promoting the effectiveness of feature representation. One common type of feature enhancement approaches for SR tasks is attention mechanism, including channel attention (Hu et al., 2018), spatial attention (Hu et al., 2019), and channel-spatial attention (Niu et al., 2020), as well as prior-guided non-local attention (Mei et al., 2023) and large kernel attention (Guo et al., 2023a; Li et al., 2025c) etc. Another more direct method involves partially shifting feature channels through primitive data movement with negligible cost. For instance, Zhang et al. (Zhang et al., 2023) proposed the PCS strategy to shift partial channels, which can intuitively enlarge the ERF of the model. Zhao et al. (Zhao et al., 2024) introduced the SLKA module, integrating channel shifting and large kernel attention to further expand the ERF. However, these models only performed fixed-direction and fixed-amplitude shifts on grouped channels, failing to thoroughly exploit the potential of channel shifting. Therefore, we designed a HFFE module for more comprehensive feature enhancement with channel-wise shifting and spatial MS-LKA.

2.3 Fourier-Domain Learning for Image Restoration

As a fundamental tool for spectral analysis, the fast Fourier transform (FFT) provides unique benefits in modeling global signal dependencies, leading to its broad adoption in various visual tasks. Mao et al. (Mao et al., 2021) devised a ResFFT module that can integrate LF and HF residual information simultaneously. Guo et al. (Guo et al., 2023b) proposed a window-based frequency channel attention that utilizes FFT to exploit richer global information. Similarly, Chen et al. (Chen et al., 2023a) combined Swin Transformer layers with fast Fourier convolution (FFC) to demodulate both local and global features. Wang et al. (Wang et al., 2023a) conducted mutual learning between frequency and spatial domains to boost the performance of face super-resolution (FSR). And Wang et al. (Wang et al., 2024a) developed a TSFNet model to combine spatial and frequency information from coarse to fine, which progressively refined the result of RSISR. These studies illustrate the efficacy of Fourier-domain learning in image restoration. However, current practice for integrating spatial-frequency features mainly resort to simple operations like concat or element-wise addition, failing to fully explore the synergy between the spatial and Fourier domains.

3 Methodology

3.1 Overall Architecture

The overall structure of our SFSN is demonstrated in Fig. 2, which follows the typical paradigm consisting of shallow feature extraction, deep feature extraction, as well as image restoration. Let $\mathbf{x} \in \mathbb{R}^{H \times W \times 3}$ represent the input, and $\mathbf{y} \in \mathbb{R}^{rH \times rW \times 3}$ to be the output of the model, where H and

Table 1: Details of the datasets. "Res." stands for the spatial resolution of pixels (m/pixel).

Datasets	Division			Size	Classes	Res.
	Train	Valid	Test			
UCMerced	945	105	1050	256^2	21	0.3
RSSCN7	1120	280	1400	400^2	7	/
AID	7850	150	2000	600^2	30	0.5

Table 2: Ablation study of the proposed SFSB on UCMerced with SR×2.

Variant	Params [K]	FLOPs [G]	UCMerced	
			PSNR	SSIM
HFFE + HFFE	692	153.4	34.44	0.9341
DDIA + DDIA	754	172.6	34.51	0.9330
DDIA + HFFE	723	163.0	34.49	0.9345
HFFE + DDIA	723	163.0	34.57	0.9350

W denote the height and width of the input image, and r stands for the scaling factor. The shallow feature $\mathbf{x}_0 \in \mathbb{R}^{H\times W\times C}$ is captured with a single 3×3 conv layer, where C denotes the number of feature channels. Then, the deep feature $\mathbf{x}_G \in \mathbb{R}^{H\times W\times C}$ can be generated via a stack of spatial frequency synergy groups (SFSG), where G represents the number of SFSG. The model yields HR image $\mathbf{y}$ as the following:

$$\mathbf{y} = \text{PixelShuffle}\big(\text{Conv}_{3\times3}\big(\mathbf{x}_0 + \text{Conv}_{3\times3}\big(\mathbf{x}_G\big)\big)\big), \tag{1}$$

where PixelShuffle$(\cdot)$ denotes the upscaling layer to enlarge the final feature to the target resolution, and Conv$_{3\times3}(\cdot)$ is 3×3 conv layers. $\mathbf{y}$ is utilized to construct L_1 loss for model training. Within each SFSG, the inference follows a similar procedure, where one SFSG includes B spatial-frequency synergy blocks (SFSBs) followed by a 3×3 conv layer and a residual shortcut.

The core components of our SFSN model, i.e., HFFE and DDIA, are contained within the SFSB. Together with SGFN (Chen et al., 2023b), they constitute two building units akin to the Transformer, as shown in Fig. 2. Suppose the input of the first unit is $\mathbf{x}_t$ and the output is $\mathbf{z}_t$, then the mapping can be formulated as (t means "temporary"):

$$\mathbf{z}_t = \mathcal{S}(\text{LN}(\mathbf{y}_t)) + \mathbf{y}_t, \;\; \mathbf{y}_t = \mathcal{H}(\text{LN}(\mathbf{x}_t)) + \mathbf{x}_t, \tag{2}$$

where $\mathbf{y}_t$ implies an intermediate feature, and LN$(\cdot)$ denotes layer normalization. $\mathcal{H}(\cdot)$ and $\mathcal{S}(\cdot)$ represent the mappings of HFFE and SGFN (Chen et al., 2023b), respectively. Similarly, the second unit with DDIA can be written as:

$$\mathbf{z}_t = \mathcal{S}(\text{LN}(\mathbf{y}_t)) + \mathbf{y}_t, \;\; \mathbf{y}_t = \mathcal{D}(\text{LN}(\mathbf{x}_t)) + \mathbf{x}_t, \tag{3}$$

where $\mathcal{D}(\cdot)$ stands for the function of DDIA.

3.2 Holistic Fusion Feature Enhancement

The HFFE is designed to comprehensively enhance features from both channel and spatial dimensions, where channel-wise enhancement is achieved through AdaCS, and spatial enhancement is in virtue of MS-LKA. The detailed structure of HFFE is illustrated in Fig. 3.

AdaCS: Given a temporary feature $\mathbf{x}_t \in \mathbb{R}^{H\times W\times C}$, AdaCS is devised to learn two shifting amplitudes, Δh and Δw, for each channel of $\mathbf{x}_t$. The structure of our AdaCS is presented in Fig. 3, where $\mathbf{s} \in \mathbb{R}^{C\times 2}$ stands for the shifting vector containing all amplitudes of C channels. The shifting vector $\mathbf{s}$ consists of two parts: (1) the shifting directions are learned by the network using a Sign$(\cdot)$ function; and (2) the shifting magnitudes are randomly assigned via a Gaussian $\mathcal{N}(\mu, \sigma)$. The procedure of obtaining $\mathbf{s}$ can be described as:

$$\mathbf{y}_t = \text{GAP}(\mathbf{x}_t), \;\; \mathbf{z}_t = \text{PWConv}(\text{ReLU}(\text{PWConv}(\mathbf{y}_t))), \;\; \mathbf{s} = \text{Sign}(\mathbf{z}_t) \otimes \mathcal{N}(\mu, \sigma), \tag{4}$$

where PWConv$(\cdot)$ denotes a 1×1 point-wise conv layer, and GAP$(\cdot)$ implies global average pooling. μ and σ indicate the mean and standard deviation of the Gaussian. We implement channel-wise shifting on $\mathbf{x}_t$ via bilinear interpolation to deal with data movement in non-integer grids. The final output of our AdaCS can be expressed as:

$$\text{AdaCS}(\mathbf{x}_t) = \text{PWConv}(\text{CS}(\mathbf{x}_t, \mathbf{s})), \tag{5}$$

where CS$(\mathbf{x}_t, \mathbf{s})$ means to shift $\mathbf{x}_t$ with the shifting vector $\mathbf{s}$ using bilinear interpolation. It is noteworthy that restricting the model to learn only the shifting directions helps reduce training complexity, while obtaining the shifting magnitudes with Gaussian sampling provides operational flexibility that permits explicit control over the shifting range. Thereby, our AdaCS enables arbitrary-magnitude shifts for non-grouped channels, significantly different from existing approaches, as shown in Fig. 5.

Table 3: Ablation study of our HFFE on UCMerced with SR×2. For convenience, we use $\mathbf{B}_1$, $\mathbf{B}_2$ and $\mathbf{B}_3$ to represent the 1st, 2nd and 3rd LKA branches (refer to Fig. 3), respectively. Please note that if only one LKA branch is deployed, then there is no channel splitting.

Metrics	Full HFFE	w/o HFFE	w/o AdaCS	AdaCS → CS	LKA Branches					
					$\mathbf{B}_1$	$\mathbf{B}_2$	$\mathbf{B}_3$	$\mathbf{B}_1+\mathbf{B}_2$	$\mathbf{B}_1+\mathbf{B}_3$	$\mathbf{B}_2+\mathbf{B}_3$
Params [K]	723	629	693	718	717	728	724	723	721	726
FLOPs [G]	163.0	143.5	158.2	162.9	161.7	164.1	163.3	162.9	162.5	163.7
PSNR [dB]	34.57	34.39	34.49	34.52	34.53	34.51	34.52	34.54	34.55	34.53
SSIM	0.9350	0.9335	0.9342	0.9347	0.9347	0.9344	0.9346	0.9346	0.9348	0.9341

MS-LKA: LSKNet (Li et al., 2023) conducted a large kernel selection mechanism to enhance features through leveraging the prior of RSI that the contextual information for different objects is very different. We take a further step for this from a multi-scale perspective, as shown in Fig. 3. For a feature $\mathbf{x}_t$ that has freshly undergone the process of our AdaCS, it is evenly divided into three sub-features $\mathbf{x}_t^1$, $\mathbf{x}_t^2$, and $\mathbf{x}_t^3$ along the channel dimension:

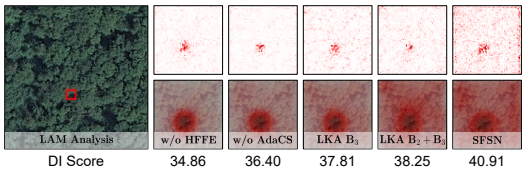

Figure 6: LAM results of different variants of our SFSN on "forest76.tif" from UCMerced.

$$[\mathbf{x}_t^1, \mathbf{x}_t^2, \mathbf{x}_t^3] = \text{Split}(\text{AdaCS}(\mathbf{x}_t)). \tag{6}$$

Each sub-feature is then enhanced by a LKA branch: $\hat{\mathbf{x}}_t^i = \text{LKA}(\mathbf{x}_t^i)$, $i = 1, 2, 3$. We employ two decomposed depth-wise convolutions (DWConv) with different kernel sizes or dilation rates to extract features within each LKA:

$$\mathbf{m}_1^i = \text{DWConv}(\mathbf{x}_t^i), \quad \mathbf{m}_2^i = \text{DWConv}(\mathbf{m}_1^i). \tag{7}$$

Let (k_1, d_1) and (k_2, d_2) denote the kernel size and dilation rate of these two layers, respectively. In our implementation, the 1st LKA branch keeps $(k_1, d_1) = (3, 3)$ and $(k_2, d_2) = (5, 3)$. For the 2nd LKA branch, $(k_1, d_1) = (3, 1)$ and $(k_2, d_2) = (7, 3)$. We set $(k_1, d_1) = (5, 1)$ and $(k_2, d_2) = (5, 5)$ for the last branch. We obtain the composite spatial attention map via $\mathbf{m}^i = \text{Concat}(\mathbf{m}_1^i, \mathbf{m}_2^i)$. The weights for selective LKA are generated by applying a PWConv and a Sigmoid activation:

$$[\mathbf{w}_1^i, \mathbf{w}_2^i] = \text{Split}(\text{Sigmoid}(\text{PWConv}(\mathbf{m}^i))), \tag{8}$$

where $\text{Split}(\cdot)$ divides these weights into two parts along the channels. The output of the i-th LKA branch is obtained via:

$$\hat{\mathbf{x}}_t^i = \text{LKA}(\mathbf{x}_t^i) = \mathbf{m}_1^i \otimes \mathbf{w}_1^i + \mathbf{m}_2^i \otimes \mathbf{w}_2^i. \tag{9}$$

The inference of the above LKA is akin to LSKNet (Li et al., 2023), but works in a simpler and more effective way. Finally, our MS-LKA yields the following:

$$\hat{\mathbf{x}}_t = \text{GeLU}(\text{PWConv}(\text{Concat}(\hat{\mathbf{x}}_t^1, \hat{\mathbf{x}}_t^2, \hat{\mathbf{x}}_t^3))). \tag{10}$$

The enhanced feature generated by our HFFE is obtained via $\mathcal{H}(\mathbf{x}_t) = \hat{\mathbf{x}}_t \otimes \mathbf{x}_t$, which can holistically promote feature effectiveness in virtue of our AdaCS and MS-LKA.

3.3 Dual-Domain Interaction Attention

The DDIA is motivated by the synergism between spatial and frequency domains, as illustrated in Fig. 4. It consists of a spatial branch that adopts a self-attention-like structure to extract features, and a FFT branch that captures frequency information with a FFT module.

Dual-Domain Feature Extraction: Given a temporary feature $\mathbf{x}_t$, we employ a self-attention-like structure to extract three spatial features $\mathbf{K}_t, \mathbf{Q}_t, \mathbf{V}_t \in \mathbb{R}^{H \times W \times C}$ using a PWConv followed by a DWConv, as shown in Fig. 4. The Fourier feature $\mathbf{F}_t$ is captured by a FFT module: $\mathbf{F}_t = \mathcal{F}(\mathbf{x}_t) \in \mathbb{R}^{H \times W \times C}$, where $\mathcal{F}(\cdot)$ denotes the mapping of the module. Let $\mathbf{y}_t = \text{FFT}(\mathbf{x}_t)$ to be the Fourier transform of $\mathbf{x}_t$, then the procedure of generating $\mathbf{F}_t$ can be formulated as:

$$\mathbf{z}_t = \text{PWConv}(\text{ReLU}(\text{PWConv}(\mathbf{y}_t))), \quad \mathbf{F}_t = \mathbf{x}_t \otimes \text{iFFT}(\mathbf{y}_t + \mathbf{z}_t), \tag{11}$$

where $\text{iFFT}(\cdot)$ is the inverse FFT. This process is depicted in the FFT module of Fig. 4.

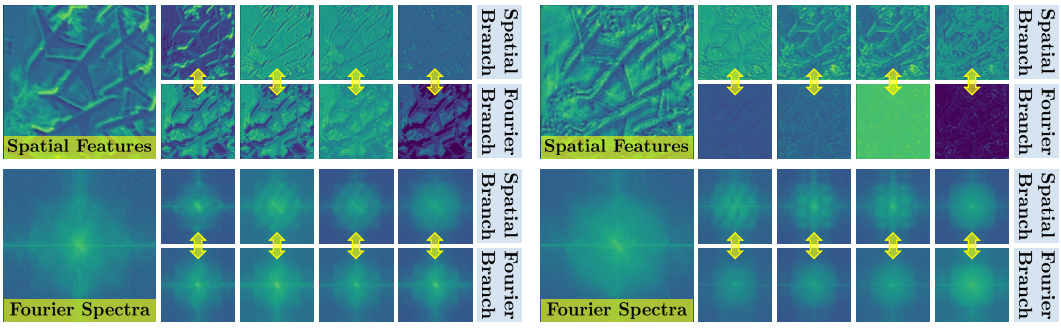

(a) The 1st DDIA (b) The 9th DDIA

Figure 7: The visualization of spatial features and Fourier spectra for the 1st and 9th DDIA modules of our SFSN model. The testing image is "airplane87.tif" from UCMerced (Yang & Newsam, 2010).

Dual-Domain Feature Interaction: All features mentioned above are reshaped into $\mathbb{R}^{HW\times C}$ for feature interaction. We first obtain a non-negative similarity matrix $\mathbf{M}\in\mathbb{R}^{C\times C}$ through:

$$\mathbf{M}=\mathrm{ReLU}\big[\mathcal{R}(\mathbf{Q}_t)^T\cdot\mathcal{R}(\mathbf{K}_t)/\sqrt{d_K}\big], \tag{12}$$

where d_K is a learnable parameter that is initialized as C, and $\mathcal{R}(\cdot)$ implies an operation of tensor reshaping. Next, we fuse spatial and spectral features as following:

$$\hat{\mathbf{V}}_t=\mathcal{R}(\mathcal{R}(\mathbf{V}_t)\cdot\mathbf{M}),\quad \hat{\mathbf{F}}_t=\mathcal{R}(\mathcal{R}(\mathbf{F}_t)\cdot\mathbf{M}). \tag{13}$$

Then we get a new feature for the spatial branch:

$$\tilde{\mathbf{V}}_t=\hat{\mathbf{V}}_t\otimes\big[\mathrm{Squeeze}\big(\mathrm{Concat}\big(\hat{\mathbf{V}}_t,\hat{\mathbf{F}}_t\big)\big)+1\big]=\hat{\mathbf{V}}_t\otimes\mathrm{Squeeze}\big(\mathrm{Concat}\big(\hat{\mathbf{V}}_t,\hat{\mathbf{F}}_t\big)\big)+\hat{\mathbf{V}}_t, \tag{14}$$

where $\mathrm{Squeeze}(\cdot)$ is composed of two PWConv layers, with a ReLU activation sandwiched between them. Please note that +1 implicitly indicates a residual shortcut. Similarly, a new spectral feature is produced by $\tilde{\mathbf{F}}_t=\mathcal{F}(\hat{\mathbf{F}}_t+\mathbf{F}_t)$.

Dual-Domain Feature Integration: Subsequently, we fuse $\tilde{\mathbf{V}}_t$ and $\tilde{\mathbf{F}}_t$ through a simple feature scaling. We first obtain two weights for feature integration as following:

$$\mathbf{w}_t^v=e^{\tilde{\mathbf{V}}_t}/(e^{\tilde{\mathbf{V}}_t}+e^{\tilde{\mathbf{F}}_t}),\qquad \mathbf{w}_t^f=e^{\tilde{\mathbf{F}}_t}/(e^{\tilde{\mathbf{V}}_t}+e^{\tilde{\mathbf{F}}_t}). \tag{15}$$

This is conducted by concatenating $\tilde{\mathbf{V}}_t$ and $\tilde{\mathbf{F}}_t$ along a new dimension and feeding them into a softmax function. So the outputs of feature integration, which is also the final output of our DDIA $\mathcal{D}(\mathbf{x}_t)$, can be expressed as: $\mathcal{D}(\mathbf{x}_t)=\mathrm{PWConv}\big(\mathbf{w}_t^v\cdot\tilde{\mathbf{V}}_t+\mathbf{w}_t^f\cdot\tilde{\mathbf{F}}_t\big)$.

4 Experiment

4.1 Datasets and Metrics

We employ three public datasets for evaluation, i.e., AID (Xia et al., 2017), RSSCN7 (Zou et al., 2015), and UCMerced (Yang & Newsam, 2010), and the detailed information for them is shown in Table 1. We evaluate the quantitative performance of the compared approaches through Peak Signal-to-Noise Ratio (PSNR) and Structural Similarity (SSIM) (Wang et al., 2004).

4.2 Implementation Details

The numbers of SFSGs, SFSBs and feature channels are set to 3, 3, and 48 respectively, and we use 6 heads for self-attention. The ratio of channel expansion for the SGFN (Chen et al., 2023b) is set to 6. All versions of our SFSN are trained with a LR patch size of 64×64 (HR patch size relies on scaling factors) for 500K iterations using a batch size of 8. We train our models using the Adam optimizer (Adam et al., 2014) with its default parameter settings. All models are implemented with PyTorch and trained on a workstation with 4 NVIDIA GeForce RTX A5000 GPUs. Besides, the FLOPs of the models are obtained based on HR images with a spatial resolution of 1280×720 pixels.

4.3 Ablation Study

In this section, we validate the effectiveness of the proposed components from coarse to fine. For fair comparisons, we implement all ablation experiments using the same settings as the proposed SFSN, using UCMerced dataset with SR×2 as the testing dataset.

Components of SFSB: We compare three variants of SFSB regarding the combination of HFFE and DDIA, as exhibited in Table 2. It can be seen that even though SFSB results in moderate parameters and FLOPs, it illustrates the best SR performance. Moreover, comparing rows #3 and #4 reveals that performing feature enhancement prior to dual-domain feature interaction benefits model inference.

Table 4: Ablation study on our DDIA with SR×2. **A**: Self-Attention; **B**: FFT Branch; **C**: Scaling; **D**: Interaction; **E**: Squeeze.

A	B	C	D	E	Params [K]	FLOPs [G]	UCMerced PSNR	UCMerced SSIM
✗	✗	✗	✗	✗	598	133.9	34.35	0.9332
✓	✗	✗	✗	✗	693	155.7	34.40	0.9335
✓	✓	✗	✗	✗	715	160.7	34.45	0.9344
✓	✓	✓	✗	✗	715	161.2	34.47	0.9347
✓	✓	✓	✓	✗	715	161.8	34.53	0.9348
✓	✓	✓	✓	✓	723	163.0	34.57	0.9350

Effectiveness of HFFE: To demonstrate the effectiveness of our HFFE, we simply remove it from SFSB and this results in a PSNR degradation of 0.18dB, as shown in Table 3. To inspect the effect of our AdaCS, we conduct experiments by removing it or replacing it with CS (Zhao et al., 2024), which leads to the results of 34.49 dB and 34.52 dB. Moreover, we implement six variants for MS-LKA: the first three variants for a single scale and the last three for two scales. The results in Table 3 prove that progressively increasing scale diversity generally leads to performance gains.

Effectiveness of DDIA: The DDIA module can be regarded as being composed of 5 components: Self-attention, FFT branch, Scaling, Interaction and Squeeze, as shown in Table 4 and Fig.4. The baseline without any component (i.e., without DDIA) achieves a PSNR value of 34.35 dB. Deploying SA on this basic model results in gains of 0.05 dB and further integration of FFT branch delivers an extra increase of 0.05 dB. Other components also contribute to the performance of the model to some extent. The results collectively validate the efficacy of the proposed DDIA.

4.4 LAM Analysis and Feature Visualization

LAM Analysis on HFFE: We leverage local attribution map (LAM) (Gu & Dong, 2021) to demonstrate the contribution of our HFFE to feature enhancement, which quantifies the impact of local regions in LR images on SR results. Fig. 6 clarifies that our HFFE and its components significantly contribute to the perception of the model to the surrounding information, which can also be verified through the diffusion indexes (DI) below each comparative group.

Feature Visualization of DDIA: RSI images often exhibit intricate texture distributions and varying scales of objects (Wang et al., 2023c), yet they also involve fewer extremely HF details commonly found in natural images, which means that the main features of RSI images may be distributed in certain spectral bands.

We visualize the internal features of our DDIA in the first and last SFSBs, as shown in Fig. 7. For each comparison group, the 1st and 2nd rows represent the spatial and Fourier branches, respectively. The 2×4 small images correspond to the average feature maps of $\mathbf{V}_t/\mathbf{F}_t$, $\hat{\mathbf{V}}_t/\hat{\mathbf{F}}_t$, $\tilde{\mathbf{V}}_t/\tilde{\mathbf{F}}_t$, and $\mathbf{w}_t^v \cdot \tilde{\mathbf{V}}_t/\mathbf{w}_t^f \cdot \tilde{\mathbf{F}}_t$, from left to right. The large image in each comparison group is the input feature or its Fourier spectrum of each DDIA. It can be seen that the Fourier branch helps to modulate the features of the spatial branch in some specific spectral bands, allowing the model to gradually learn more refined structural and spectral details.

4.5 Comparison with Advanced Methods

We compare our SFSN with several advanced SR methods including: SwinIR (Liang et al., 2021), TransENet (Lei et al., 2021), FeNet (Wang et al., 2022), OmniSR (Wang et al., 2023b), SRFormer (Zhou et al., 2023), MAN (Wang et al., 2024b), SRConvNet (Li et al., 2025b), MambaIR (Guo et al., 2024), SSIU (Ni et al., 2025).

Quantitative Comparison: Table 5 shows the quantitative results of compared approaches. As can be seen, our SFSN presents the best performance across all benchmark datasets for various

Table 5: Quantitative results of advanced SISR models. SFSN+ represents the enhanced version of our model with geometric self-ensemble (Lim et al., 2017). The best and second-best results are marked in red and blue, respectively.

Scales	SISR Models	Annual	Params [K]	FLOPs [G]	UCMerced		RSSCN7		AID	
					PSNR	SSIM	PSNR	SSIM	PSNR	SSIM
SR×2	SwinIR-L	ICCV2021	910	252.9	34.48	0.9343	30.18	0.8082	35.46	0.9378
	TransENet	TGRS2022	37311	550.5	34.05	0.9294	30.08	0.8040	35.40	0.9372
	FeNet	TGRS2022	351	77.9	33.95	0.9284	30.05	0.8033	35.33	0.9364
	OmniSR	CVPR2023	772	172.1	34.16	0.9303	30.11	0.8052	35.50	0.9383
	SRFormer-L	ICCV2023	853	236.2	34.53	0.9347	30.23	0.8101	35.52	0.9384
	MAN-L	CVPR2024	823	184.0	34.44	0.9341	30.18	0.8093	35.53	0.9389
	MambaIR-L	ECCV2024	905	334.2	34.45	0.9334	30.22	0.8098	35.51	0.9381
	SRConvNet-L	IJCV2025	885	160.1	34.35	0.9333	30.20	0.8090	35.50	0.9381
	SSIU	TIP2025	778	164.5	34.50	0.9344	30.22	0.8094	35.52	0.9384
	SFSN (Ours)	—	723	163.0	34.57	0.9350	30.26	0.8113	35.56	0.9397
	SFSN+ (Ours)	—	723	163.0	34.75	0.9365	30.30	0.8123	35.67	0.9401
SR×3	SwinIR-L	ICCV2021	918	114.5	30.15	0.8466	28.05	0.7081	31.53	0.8596
	TransENet	TGRS2022	37496	357.5	29.90	0.8397	28.02	0.7054	31.50	0.8588
	FeNet	TGRS2022	357	35.2	29.80	0.8379	27.97	0.7031	31.33	0.8550
	OmniSR	CVPR2023	780	78.0	29.99	0.8403	28.04	0.7061	31.53	0.8596
	SRFormer-L	ICCV2023	861	104.8	30.23	0.8502	28.07	0.7089	31.57	0.8607
	MAN-L	CVPR2024	832	81.3	30.08	0.8446	28.02	0.7072	31.53	0.8607
	MambaIR-L	ECCV2024	913	148.5	30.15	0.8468	28.08	0.7097	31.56	0.8601
	SRConvNet-L	IJCV2025	906	74.8	29.89	0.8382	28.02	0.7063	31.53	0.8595
	SSIU	TIP2025	799	75.1	30.17	0.8499	28.06	0.7082	31.57	0.8609
	SFSN (Ours)	—	729	71.9	30.29	0.8519	28.10	0.7102	31.60	0.8622
	SFSN+ (Ours)	—	729	71.9	30.44	0.8550	28.14	0.7115	31.67	0.8628
SR×4	SwinIR-L	ICCV2021	930	65.2	27.78	0.7662	26.83	0.6391	29.35	0.7883
	TransENet	TGRS2022	37459	268.0	27.78	0.7635	26.81	0.6372	29.44	0.7912
	FeNet	TGRS2022	366	20.4	27.59	0.7538	26.80	0.6367	29.16	0.7812
	OmniSR	CVPR2023	792	45.0	27.80	0.7637	26.85	0.6388	29.19	0.7829
	SRFormer-L	ICCV2023	873	62.8	27.83	0.7680	26.84	0.6400	29.39	0.7895
	MAN-L	CVPR2024	921	47.1	27.68	0.7638	26.77	0.6382	29.35	0.7891
	MambaIR-L	ECCV2024	924	84.6	27.77	0.7666	26.84	0.6400	29.37	0.7882
	SRConvNet-L	IJCV2025	902	45.5	27.61	0.7618	26.79	0.6366	29.33	0.7873
	SSIU	TIP2025	794	49.6	27.75	0.7652	26.83	0.6392	29.40	0.7894
	SFSN (Ours)	—	738	41.6	27.89	0.7699	26.87	0.6419	29.46	0.7913
	SFSN+ (Ours)	—	738	41.6	28.09	0.7747	26.92	0.6437	29.51	0.7923

scale factors. Notably, it achieves the best results with second-lowest model parameters and FLOPs, striking a better trade-off between model performance and overhead. A similar conclusion can also be drawn from Fig. 1.

Qualitative Comparison: We present the visual comparison of these methods in Fig. 8, where two images from AID and UCMerced are used for evaluation with SR×4. It can be observed that our SFSN model is capable of reconstructing the latent contours of the objects more reliably, which poses a significant impact on recognition, detection and counting tasks. However, most other methods fail to correctly recover this scenario. For instance, the results of some SR methods erroneously blend the dock and small boats together, such as SwinIR, FeNet, SRFormer and SSIU.

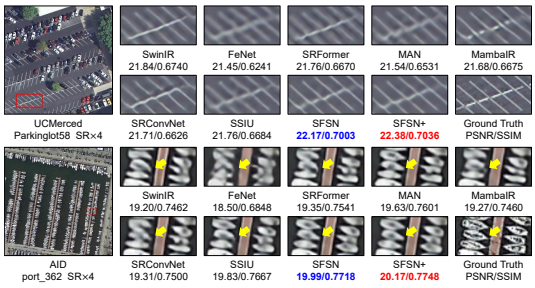

Figure 8: Visual results of compared RSISR models with SR×4. The best and second-best results are marked in red and blue, respectively.

5 Conclusion

In this work, we propose a lightweight SFSN for the RSISR task, which comprehensively lifts model capability through the perspectives of feature enhancement and the synergism between spatial and frequency domains. We leverage AdaCS and MS-LKA operating on channel and spatial dimensions respectively to comprehensively enhance features, while the spatial-frequency domain synergism is implemented via an attention mechanism assisted by a Fourier branch. Extensive experiments demonstrate that, with the aid of holistic feature enhancement, the proposed SFSN model effectively alleviates the problem of long-range dependencies and spatial relationship modeling confronted by single domain processing in RSISR tasks, and it also strikes a better compromise between model performance and complexity.

REFERENCES

Kingma DP Ba J Adam et al. A method for stochastic optimization, 2014.

Wendy M Calvin, Elizabeth F Littlefield, and Christopher Kratt. Remote sensing of geothermal-related minerals for resource exploration in nevada. *Geothermics*, 53:517–526, 2015.

Ke Chen, Liangyan Li, Huan Liu, Yunzhe Li, Congling Tang, and Jun Chen. Swinfsr: Stereo image super-resolution using swinir and frequency domain knowledge. In *Proceedings of the IEEE/CVF Conference on Computer Vision and Pattern Recognition*, pp. 1764–1774, 2023a.

Zheng Chen, Yulun Zhang, Jinjin Gu, Linghe Kong, Xiaokang Yang, and Fisher Yu. Dual aggregation transformer for image super-resolution. In *Proceedings of the IEEE/CVF International Conference on Computer Vision*, pp. 12312–12321, 2023b.

Chao Dong, Chen Change Loy, Kaiming He, and Xiaoou Tang. Learning a deep convolutional network for image super-resolution. In *Computer Vision–ECCV 2014: 13th European Conference, Zurich, Switzerland, September 6-12, 2014, Proceedings, Part IV 13*, pp. 184–199, 2014.

Xiaoyu Dong, Xu Sun, Xiuping Jia, Zhihong Xi, Lianru Gao, and Bing Zhang. Remote sensing image super-resolution using novel dense-sampling networks. *IEEE Transactions on Geoscience and Remote Sensing*, 59(2):1618–1633, 2020.

Daniel Glasner, Shai Bagon, and Michal Irani. Super-resolution from a single image. In *IEEE International Conference on Computer Vision*, pp. 349–356, 2009.

Jinjin Gu and Chao Dong. Interpreting super-resolution networks with local attribution maps. In *Proceedings of the IEEE/CVF Conference on Computer Vision and Pattern Recognition*, pp. 9199–9208, 2021.

Hang Guo, Jinmin Li, Tao Dai, Zhihao Ouyang, Xudong Ren, and Shu-Tao Xia. Mambair: A simple baseline for image restoration with state-space model. In *European Conference on Computer Vision*, pp. 222–241, 2024.

Hang Guo, Yong Guo, Yaohua Zha, Yulun Zhang, Wenbo Li, Tao Dai, Shu-Tao Xia, and Yawei Li. Mambairv2: Attentive state space restoration. In *Proceedings of the Computer Vision and Pattern Recognition Conference*, pp. 28124–28133, 2025.

Meng-Hao Guo, Cheng-Ze Lu, Zheng-Ning Liu, Ming-Ming Cheng, and Shi-Min Hu. Visual attention network. *Computational Visual Media*, 9(4):733–752, 2023a.

Shi Guo, Hongwei Yong, Xindong Zhang, Jianqi Ma, and Lei Zhang. Spatial-frequency attention for image denoising, 2023b.

Juan Mario Haut, Mercedes Eugenia Paoletti, Rubén Fernández-Beltran, Javier Plaza, Antonio Plaza, and Jun Li. Remote sensing single-image superresolution based on a deep compendium model. *IEEE Geoscience and Remote Sensing Letters*, 16(9):1432–1436, 2019.

Jie Hu, Li Shen, and Gang Sun. Squeeze-and-excitation networks. In *Proceedings of the IEEE/CVF Conference on Computer Vision and Pattern Recognition*, pp. 7132–7141, 2018.

Yanting Hu, Jie Li, Yuanfei Huang, and Xinbo Gao. Channel-wise and spatial feature modulation network for single image super-resolution. *IEEE Transactions on Circuits and Systems for Video Technology*, 30(11):3911–3927, 2019.

Xudong Kang, Puhong Duan, Jier Li, and Shutao Li. Efficient swin transformer for remote sensing image super-resolution. *IEEE Transactions on Image Processing*, 33:6367–6379, 2024.

Sen Lei and Zhenwei Shi. Hybrid-scale self-similarity exploitation for remote sensing image super-resolution. *IEEE Transactions on Geoscience and Remote Sensing*, 60:1–10, 2021.

Sen Lei, Zhenwei Shi, and Zhengxia Zou. Super-resolution for remote sensing images via local–global combined network. *IEEE Geoscience and Remote Sensing Letters*, 14(8):1243–1247, 2017.

Sen Lei, Zhenwei Shi, and Wenjing Mo. Transformer-based multistage enhancement for remote sensing image super-resolution. *IEEE Transactions on Geoscience and Remote Sensing*, 60:1–11, 2021.

Ao Li, Le Zhang, Yun Liu, and Ce Zhu. Exploring frequency-inspired optimization in transformer for efficient single image super-resolution. *IEEE Transactions on Pattern Analysis and Machine Intelligence*, 47(4):3141–3158, 2025a.

Feng Li, Runmin Cong, Jingjing Wu, Huihui Bai, Meng Wang, and Yao Zhao. Srconvnet: A transformer-style convnet for lightweight image super-resolution. *International Journal of Computer Vision*, 133(1):173–189, 2025b.

Yaohua Li, Xiaole Zhao, Xiaobo Zhang, Yan Yang, and Tianrui Li. Long-range multi-scale fusion for efficient single image super-resolution. In *IEEE International Conference on Acoustics, Speech and Signal Processing*, pp. 1–5, 2025c.

Yuxuan Li, Qibin Hou, Zhaohui Zheng, Ming-Ming Cheng, Jian Yang, and Xiang Li. Large selective kernel network for remote sensing object detection. In *Proceedings of the IEEE/CVF International Cconference on Computer Vision*, pp. 16794–16805, 2023.

Jingyun Liang, Jiezhang Cao, Guolei Sun, Kai Zhang, Luc Van Gool, and Radu Timofte. Swinir: Image restoration using swin transformer. In *Proceedings of the IEEE/CVF International Conference on Computer Vision*, pp. 1833–1844, 2021.

Bee Lim, Sanghyun Son, Heewon Kim, Seungjun Nah, and Kyoung Mu Lee. Enhanced deep residual networks for single image super-resolution. In *Proceedings of the IEEE Conference on Computer Vision and Pattern Recognition Workshops*, pp. 136–144, 2017.

Xintian Mao, Yiming Liu, Wei Shen, Qingli Li, and Yan Wang. Deep residual fourier transformation for single image deblurring, 2021.

Yiqun Mei, Yuchen Fan, Yulun Zhang, Jiahui Yu, Yuqian Zhou, Ding Liu, Yun Fu, Thomas S Huang, and Humphrey Shi. Pyramid attention network for image restoration. *International Journal of Computer Vision*, 131(12):3207–3225, 2023.

Zhangkai Ni, Yang Zhang, Wenhan Yang, Hanli Wang, Shiqi Wang, and Sam Kwong. Structural similarity-inspired unfolding for lightweight image super-resolution. *IEEE Transactions on Image Processing*, 34:3861–3872, 2025.

Ben Niu, Weilei Wen, Wenqi Ren, Xiangde Zhang, Lianping Yang, Shuzhen Wang, Kaihao Zhang, Xiaochun Cao, and Haifeng Shen. Single image super-resolution via a holistic attention network. In *European Conference on Computer Vision*, pp. 191–207, 2020.

JiannYeou Rau, JyunPing Jhan, and YaChing Hsu. Analysis of oblique aerial images for land cover and point cloud classification in an urban environment. *IEEE Transactions on Geoscience and Remote Sensing*, 53(3):1304–1319, 2014.

Ashish Vaswani, Noam Shazeer, Niki Parmar, Jakob Uszkoreit, Llion Jones, Aidan N. Gomez, Lukasz Kaiser, and Illia Polosukhin. Attention is all you need. In *Advances in Neural Information Processing Systems*, pp. 5998–6008, 2017.

Chenyang Wang, Junjun Jiang, Zhiwei Zhong, and Xianming Liu. Spatial-frequency mutual learning for face super-resolution. In *Proceedings of the IEEE/CVF Conference on Computer Vision and Pattern Recognition*, pp. 22356–22366, 2023a.

Hang Wang, Xuanhong Chen, Bingbing Ni, Yutian Liu, and Jinfan Liu. Omni aggregation networks for lightweight image super-resolution. In *Proceedings of the IEEE/CVF Conference on Computer Vision and Pattern Recognition*, pp. 22378–22387, 2023b.

Hongyuan Wang, Shuli Cheng, Yongming Li, and Anyu Du. Lightweight remote-sensing image super-resolution via attention-based multilevel feature fusion network. *IEEE Transactions on Geoscience and Remote Sensing*, 61:1–15, 2023c.

Jiarui Wang, Binglu Wang, Xiaoxu Wang, Yongqiang Zhao, and Teng Long. Hybrid attention-based u-shaped network for remote sensing image super-resolution. *IEEE Transactions on Geoscience and Remote Sensing*, 61:1–15, 2023d.

Jiarui Wang, Yuting Lu, Shunzhou Wang, Binglu Wang, Xiaoxu Wang, and Teng Long. Two-stage spatial-frequency joint learning for large-factor remote sensing image super-resolution. *IEEE Transactions on Geoscience and Remote Sensing*, 62:1–13, 2024a.

Yan Wang, Yusen Li, Gang Wang, and Xiaoguang Liu. Multi-scale attention network for single image super-resolution. In *Proceedings of the IEEE/CVF Conference on Computer Vision and Pattern Recognition*, pp. 5950–5960, 2024b.

Zhenggang Wang, Qing Kang, Yijia Xun, Zhiqiang Shen, and Changbin Cui. Military reconnaissance application of high-resolution optical satellite remote sensing. In *International Symposium on Optoelectronic Technology and Application 2014: Optical Remote Sensing Technology and Applications*, volume 9299, pp. 301–305, 2014.

Zheyuan Wang, Liangliang Li, Yuan Xue, Chenchen Jiang, Jiawen Wang, Kaipeng Sun, and Hongbing Ma. Fenet: Feature enhancement network for lightweight remote-sensing image super-resolution. *IEEE Transactions on Geoscience and Remote Sensing*, 60:1–12, 2022.

Zhou Wang, Alan C Bovik, Hamid R Sheikh, and Eero P Simoncelli. Image quality assessment: from error visibility to structural similarity. *IEEE Transactions on Image Processing*, 13(4):600–612, 2004.

Gui-Song Xia, Jingwen Hu, Fan Hu, Baoguang Shi, Xiang Bai, Yanfei Zhong, Liangpei Zhang, and Xiaoqiang Lu. Aid: A benchmark data set for performance evaluation of aerial scene classification. *IEEE Transactions on Geoscience and Remote Sensing*, 55(7):3965–3981, 2017.

Yi Xiao, Qiangqiang Yuan, Kui Jiang, Yuzeng Chen, Qiang Zhang, and Chia-Wen Lin. Frequency-assisted mamba for remote sensing image super-resolution. *IEEE Transactions on Multimedia*, 27:1783–1796, 2024.

Yi Yang and Shawn Newsam. Bag-of-visual-words and spatial extensions for land-use classification. In *Proceedings of the 18th SIGSPATIAL International Conference on Advances in Geographic Information Systems*, pp. 270–279, 2010.

Dongyang Zhang, Jie Shao, Xinyao Li, and Heng Tao Shen. Remote sensing image super-resolution via mixed high-order attention network. *IEEE Transactions on Geoscience and Remote Sensing*, 59(6):5183–5196, 2020.

Xiaoming Zhang, Tianrui Li, and Xiaole Zhao. Boosting single image super-resolution via partial channel shifting. In *Proceedings of the IEEE/CVF International Conference on Computer Vision*, pp. 13223–13232, 2023.

Xiaole Zhao, Linze Li, Chengxing Xie, Xiaoming Zhang, Ting Jiang, Wenjie Lin, Shuaicheng Liu, and Tianrui Li. Efficient single image super-resolution with entropy attention and receptive field augmentation. In *Proceedings of the 32nd ACM International Conference on Multimedia*, pp. 1302–1310, 2024.

Yupeng Zhou, Zhen Li, ChunLe Guo, Song Bai, Ming-Ming Cheng, and Qibin Hou. Srformer: Permuted self-attention for single image super-resolution. In *Proceedings of the IEEE/CVF International Conference on Computer Vision*, pp. 12780–12791, 2023.

Qiwei Zhu, Guojing Zhang, Xuechao Zou, Xiaoying Wang, Jianqiang Huang, and Xilai Li. Convmambasr: Leveraging state-space models and cnns in a dual-branch architecture for remote sensing imagery super-resolution. *Remote Sensing*, 16(17):3254, 2024.

Qin Zou, Lihao Ni, Tong Zhang, and Qian Wang. Deep learning based feature selection for remote sensing scene classification. *IEEE Geoscience and Remote Sensing Letters*, 12(11):2321–2325, 2015.

A APPENDIX

A.1 INTRODUCTION

We include some supplementary explanations with regard to our SFSN model, implementation details, and experimental comparisons in this document:

- **Channel Splitting**: Given the shifting vector $\mathbf{s}$, we detail how to shift the channels of intermediate features, which was omitted in the main text due to page limits.
- **Implementation Details**: We provide an explanation on the implementation of the LKA of our HFFE.
- **Ablation Study**: Due to the complex architecture of our DDIA, we elaborately show the structures of the variants in its ablation experiments.
- **Experiments**: We also add some additional experimental results here, including LAM analysis, quantitative results with other models, and extra visual comparisons.

A.2 ADDITIONAL IMPLEMENTATION DETAILS

A.3 CHANNEL SHIFTING

Within our AdaCS, we utilize $\mathrm{CS}(\mathbf{x}_t, \mathbf{s})$ to shift intermediate feature $\mathbf{x}_t$ through the shifting vector $\mathbf{s}$. The implementation details of $\mathrm{CS}(\mathbf{x}_t, \mathbf{s})$ are demonstrated in Algorithm 1. It first generates shifted coordinate grids with $\mathbf{s}$, and then performs feature shifting using bilinear interpolation.

The source code and pre-trained models of our SFSN will be publicly released on Github.

A.4 EXPERIMENTS

A.4.1 ABLATION STUDY

Explanation of Variants of MS-LKA: In the ablation study of MS-LKA, we have six variants: the first three variants use one single LKA without channel splitting (48 channels for mapping), and the last three ones employ two different LKAs, each of which possesses a half of the channels of the original feature (24 out of 48).

Explanation of Variants of DDIA: It can be seen in Fig. 9 that our DDIA consists of five components: Self-attention (**A**), FFT branch (**B**), Scaling (**C**), Interaction (**D**), Squeeze (**E**). In Fig. 9, the variant **A** indicates that only component **A** is used, and the variant **B** incorporates component **B** based on variant **A**. Similarly, the variant **C** is built through adding component **C** to the preceding variant **B**, and the variant **D** is formed by adding component **D** to the variant **C**, as shown in Fig. 10. Besides, the entire DDIA module is constructed by supplementing component **E** to the variant **D**.

A.4.2 COMPARISON EXPERIMENTS

LAM Comparison with SRConvNet: To better exhibit the performance advantages of our SFSN, we leverage LAM to conduct attribution analyses on both SFSN and the advanced SRConvNet (Li et al., 2025b). Through this side-by-side comparison, we can intuitively contrast the critical visual cues relied upon by both models during their decision-making processes, thus enabling a more comprehensive evaluation of their performance. As shown in Fig. 11, it is evident that our model is capable of reconstructing target regions through larger spatial areas. This indicates that it can leverage texture information from a broader scope than SRConvNet (Li et al., 2025b) to facilitate more accurate detail reconstruction.

More Quantitative Results: Due to the page constraint, we omitted quantitative comparisons with several representative SR models in the main document, including SRCNN (Dong et al., 2014), MHAN (Zhang et al., 2020), HSENet (Lei & Shi, 2021), and MambaIR-v2 (Guo et al., 2025). Among these models, SRCNN (Dong et al., 2014) is a pioneering work that adopted CNNs to deal with SISR tasks. MHAN (Zhang et al., 2020) and HSENet (Lei & Shi, 2021) are two representative models specifically designed for RSISR tasks. MambaIR-v2 (Guo et al., 2025) is a latest model with

Algorithm 1 Channel Shifting

Input: $\mathbf{x}_t \in \mathbb{R}^{C\times H\times W}, \quad \mathbf{s} \in \mathbb{R}^{2C}$
Output: $\mathbf{x}_t^* = \mathrm{CS}(\mathbf{x}_t, \mathbf{s}) \in \mathbb{R}^{C\times H\times W}$

$\mathbf{g} \leftarrow \mathrm{createGrid}(H, W)$ /*$1 \times H \times W \times 2$*/
$\mathbf{s} \leftarrow \mathrm{reshape}(\mathbf{s}, (C, 1, 1, 2))$
$\widetilde{\mathbf{g}} \leftarrow \mathbf{g} + \mathbf{s}$ /*Broadcast Addition*/
$\widetilde{\mathbf{g}}[..., 0] \leftarrow 2 \times \frac{\widetilde{\mathbf{g}}[..., 0]}{W-1} - 1$ /*Normalize x*/
$\widetilde{\mathbf{g}}[..., 1] \leftarrow 2 \times \frac{\widetilde{\mathbf{g}}[..., 1]}{H-1} - 1$ /*Normalize y*/
$\hat{\mathbf{g}} \leftarrow \mathrm{reshape}(\widetilde{\mathbf{g}}, (C, H, W, 2))$
$\hat{\mathbf{x}}_\mathbf{t} \leftarrow \mathrm{reshape}(\mathbf{x}_t, (C, 1, H, W))$
$\widetilde{\mathbf{x}}_\mathbf{t} \leftarrow \mathrm{gridSample}(\hat{\mathbf{x}}_\mathbf{t}, \hat{\mathbf{g}}; \mathrm{mode}=\text{“bilinear”})$
$\mathbf{x}_t^* \leftarrow \mathrm{reshape}(\widetilde{\mathbf{x}}_\mathbf{t}, (C, H, W))$
return $\mathbf{x}_t^*$

superior performance for image restoration. The additional quantitative results are provided in Table 6 of this supplementary material.

As illustrated in Table 6, it can be observed that although SRCNN (Dong et al., 2014) is highly efficient compared to other models, its performance is severely unsatisfactory. On the other hand, MHAN (Zhang et al., 2020) and HSENet (Lei & Shi, 2021) show better results, but their parameter counts and computational costs are excessively high, placing them beyond the scope of lightweight models. The model closest to our SFSN in SR performance is MambaIR-v2 (Guo et al., 2025). However, our SFSN still achieves more superior SR results with lower computational overhead, striking a better performance-efficiency equilibrium than MambaIR-v2 (Guo et al., 2025).

Additional Visual Results: To complement the qualitative results and provide more visual comparison, we exhibit extra visual results in Fig. 12, Fig. 13, Fig. 14, Fig. 15. It is observable that our method achieves superior recovery of HF information neglected by other models, which can induce blurring or artifacts within complex regions.

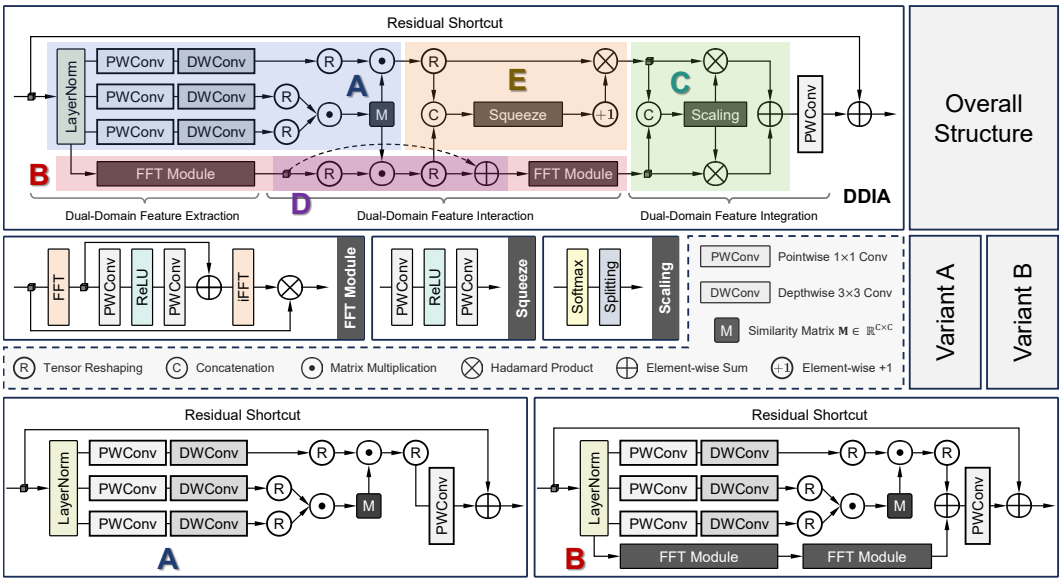

Figure 9: The variants for DDIA ablation study. We mark the main structural components of our DDIA with different colors. The variant **A** can be viewed as a simple self-attention, and the variant **B** is built by adding component **B** (i.e., the FFT branch) to the variant **A**. Other variants tested in the ablation study of our DDIA can be found in Fig. 10.

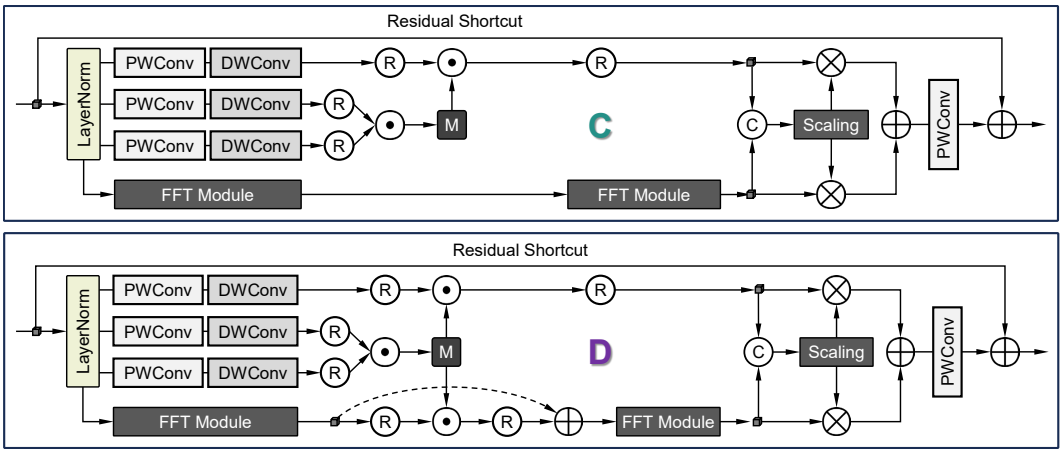

Figure 10: The variants **C** and **D** for DDIA ablation study. **C** is built by incorporating component **C** (i.e., feature scaling) into the variant **B**, and **D** is formed with component **D** (i.e., dual-domain feature interaction). When component **E** (squeeze) is adopted by the variant **D**, it then become the complete DDIA module.

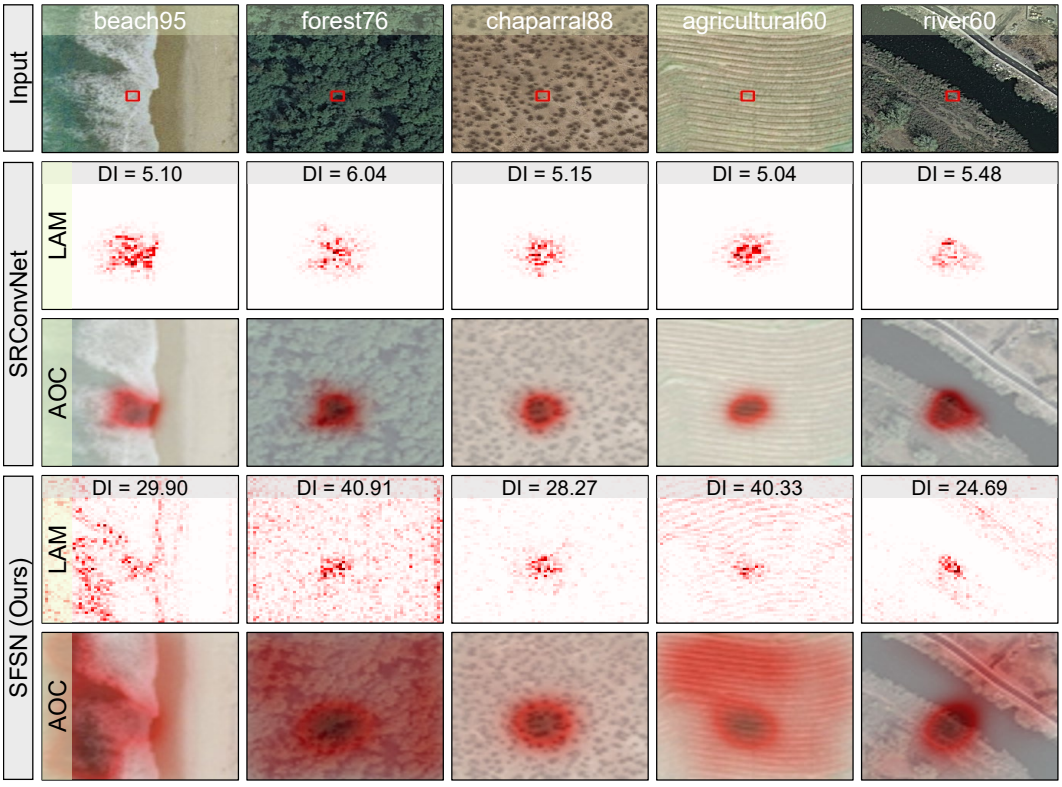

Figure 11: LAM and AOC comparison between SRConvNet (Li et al., 2025b) and the proposed SFSN on five testing images from UCMerced (Yang & Newsam, 2010).

Table 6: Quantitative results of advanced SISR models. SFSN+ represents the enhanced version of our model with geometric self-ensemble (Lim et al., 2017). The best and second-best results are marked in red and blue, respectively.

Scales	SISR Models	Annual	Params [K]	FLOPs [G]	UCMerced		RSSCN7		AID	
					PSNR	SSIM	PSNR	SSIM	PSNR	SSIM
SR×2	SRCNN	ECCV2014	57	52.7	32.94	0.9170	29.83	0.7954	34.65	0.9290
	MHAN	TGRS2020	11203	2315.6	33.92	0.9283	30.06	0.8036	35.56	0.9390
	HSENet	TGRS2022	5286	939.6	34.22	0.9327	30.15	0.8070	35.50	0.9383
	MambaIRv2-L	CVPR2025	774	286.3	34.54	0.9345	30.25	0.8104	35.54	0.9386
	SFSN (Ours)	—	723	163.0	34.57	0.9350	30.26	0.8113	35.56	0.9397
	SFSN+ (Ours)	—	723	163.0	34.75	0.9365	30.30	0.8123	35.67	0.9401
SR×3	SRCNN	ECCV2014	57	52.7	28.91	0.8132	27.77	0.6936	30.55	0.8372
	MHAN	TGRS2020	11287.5	1177.7	29.94	0.8391	28.00	0.7045	31.55	0.8603
	HSENet	TGRS2022	5470	430.5	30.04	0.8433	28.02	0.7067	31.49	0.8588
	MambaIRv2-L	CVPR2025	781	126.7	30.24	0.8491	28.08	0.7083	31.58	0.8607
	SFSN (Ours)	—	729	71.9	30.29	0.8519	28.10	0.7102	31.60	0.8622
	SFSN+ (Ours)	—	729	71.9	30.44	0.8550	28.14	0.7115	31.67	0.8628
SR×4	SRCNN	ECCV2014	57	52.7	26.92	0.7286	26.64	0.6278	28.48	0.7565
	MHAN	TGRS2020	11351	711.9	27.63	0.7581	26.79	0.6360	29.39	0.7892
	HSENet	TGRS2022	5433	270.1	27.75	0.7611	26.82	0.6378	29.32	0.7867
	MambaIRv2-L	CVPR2025	790	49.6	27.88	0.7694	26.86	0.6408	29.40	0.7894
	SFSN (Ours)	—	738	41.6	27.89	0.7699	26.87	0.6419	29.46	0.7913
	SFSN+ (Ours)	—	738	41.6	28.09	0.7747	26.92	0.6437	29.51	0.7923

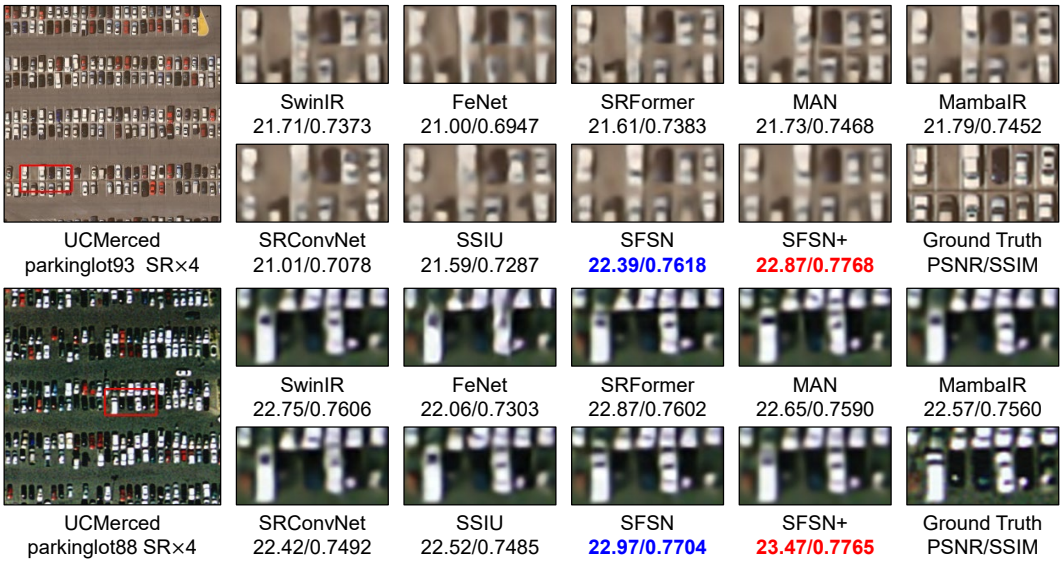

Figure 12: Visual results of compared RSISR models on two testing images from UCMerced (Yang & Newsam, 2010). The best and second-best results are marked with red and blue, respectively.

Figure 13: Visual results of compared RSISR models on two testing images from UCMerced (Yang & Newsam, 2010). The best and second-best results are marked with red and blue, respectively.

Figure 14: Visual results of several compared RSISR models on two testing images from AID (Xia et al., 2017). The best and second-best results are marked with red and blue, respectively.

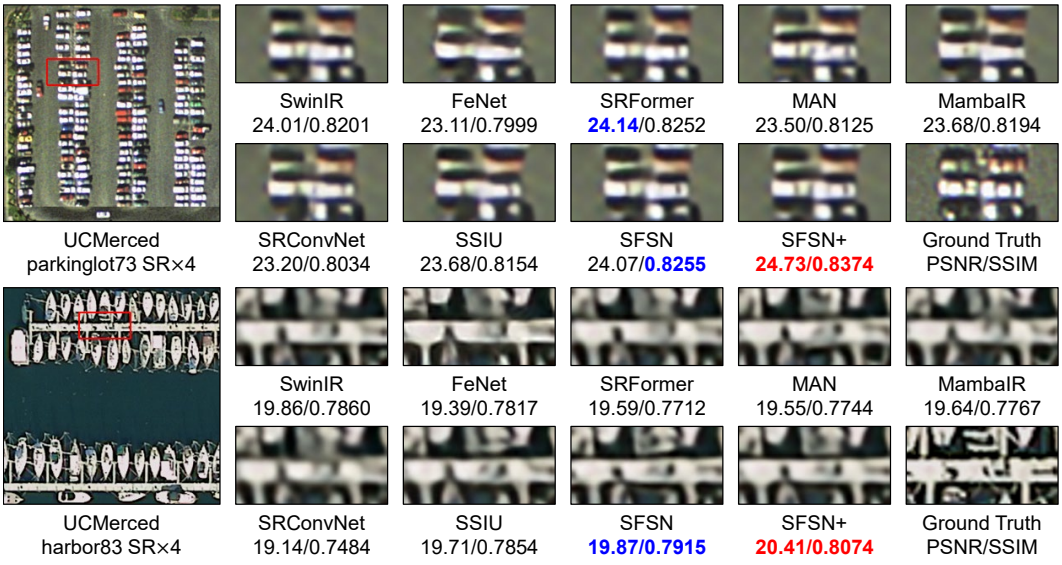

Figure 15: Visual results of compared RSISR models on two testing images from UCMerced (Yang & Newsam, 2010). The best and second-best results are marked with red and blue, respectively.